Multiple mechanisms for chlorophyll-a concentration variations in coastal upwelling regions: A case study east of Hainan Island in the South China Sea

Junyi Li [1,2,3], Min Li [1*], Chao Wang [1], Quanan Zheng [1,4], Ying Xu[3], Tianyu Zhang[1] Lingling Xie[1*]

[1] Laboratory of Coastal Ocean Variation and Disaster Prediction, Guangdong Ocean University, Zhanjiang 524088, China

[2] Key Laboratory of Climate, Sources and Environments in Continent Shelf Sea and Deep Ocean, Zhanjiang 524088, China

[3] Key Laboratory of Space Ocean Remote Sensing and Application, MNR, Beijing, 100081, China

[4] Department of Atmospheric and Oceanic Science, University of Maryland, College Park, MD 20742, USA

 Corresponding author.

E-mail address: M. Li (min_li@gdou.edu.cn), L. Xie (xiell@gdou.edu.cn);

Abstract

Using satellite observations from 2003 to 2020 and cruise observations in 2019 and 2021, this study reveals an unexpected minor role of upwelling in seasonal and interannual variations in chlorophyll-a (Chl-a) concentrations in the coastal upwelling region east of Hainan Island (UEH) in the northwestern South China Sea (NWSCS). The results show strong seasonal and interannual variability in the Chl-a concentration in the core upwelling area of the UEH. Different from the strongest upwelling in summer, the Chl-a concentration in the UEH area reaches a maximum of 1.18 mg m^{-3} in autumn and winter, with a minimum value of 0.74 mg m^{-3} in summer. The summer Chl-a concentration increases to as high as 1.0 mg m^{-3} with weak upwelling during El Niño years, whereas the maximum Chl-a concentration in October increases to 2.5 mg m^{-3} during La Niña years. The analysis of environmental factors shows that compared to the limited effects of upwelling, the along-shelf coastal current from the northern shelf and the increased precipitation are crucially important to the Chl-a concentration variation in the study area. These results provide new insights for predicting marine productivity in upwelling areas, i.e., multiple mechanisms, especially horizontal advection, should be considered in addition to the upwelling process.

Keywords: Coastal upwelling; chlorophyll-a concentration; Guangdong Coastal Current; ENSO events; EOF analysis

1 Introduction

The oceanic area with coastal upwelling is generally characterized by high productivity; it occupies only 1% of the total area of the ocean but provides more than 50% of the total marine fish harvest (Barua, 2005). High levels of biological productivity strongly influence atmosphere-ocean carbon recycling (Mcgregor et al., 2007; Xu et al., 2020). Therefore, revealing the variation in chlorophyll-a (Chl-a) in coastal upwelling areas is important to the overall health of the marine ecosystem and climate.

The upward movement of seawater may carry nutrients from the lower layer and support a high surface Chl-a concentration. Thus, the variability in Chl-a concentrations in coastal upwelling regions is proposed to be associated with that of upwelling (Jing et al., 2009). Alongshore winds, positive wind curl, tidal mixing and topography may affect upwelling processes (Hu and Wang,

45   2016). In contrast, other oceanic and atmospheric processes, such as mesoscale eddies, sub-
46   mesoscale fronts, precipitation and typhoon processes, can also induce Chl-a increments (Aoki et
47   al., 2019; Cape et al., 2019; Li et al., 2021a; Li et al., 2021b).

48   The coastal upwelling east of Hainan Island (UEH) is part of the seasonal upwelling in the
49   northwestern South China Sea (NWSCS). As shown in Figure 1, the isobaths in the shelf are
50   parallel to the continental coastline. The width of the continental shelf is approximately 100 km.
51   Outside of the continental shelf, there is a steep slope linking the shelf to the South China Sea
52   (SCS) Basin. The circulation in the coastal area east of Hainan Island (HEC) is controlled by the
53   East Asian monsoon system. In summer, the coastal current travels northeastward on the shelf
54   influenced by the southwesterly monsoon, whereas in winter, the current flows southwestward
55   (Ding et al., 2018; Jing et al., 2015). According to the Ekman transport theory, the along-shelf
56   wind induces cross-shelf transport of the surface water and thus causes coastal upwelling along the
57   coastline in summer. The UEH generally begins in April, becomes strongest in July and August,
58   and remains until September (Xie et al., 2012). The UEH is located in coastal shallow water less
59   than 100 m (Jing et al., 2015). Wind stress curl-induced Ekman pumping is considered to be
60   another crucial factor for UEH generation (Xu et al., 2020). In addition, the strong northeastward
61   current along the shelf could cause strong stratification towards the coast, and thus enhances
62   upwelling (Su et al., 2013).

63
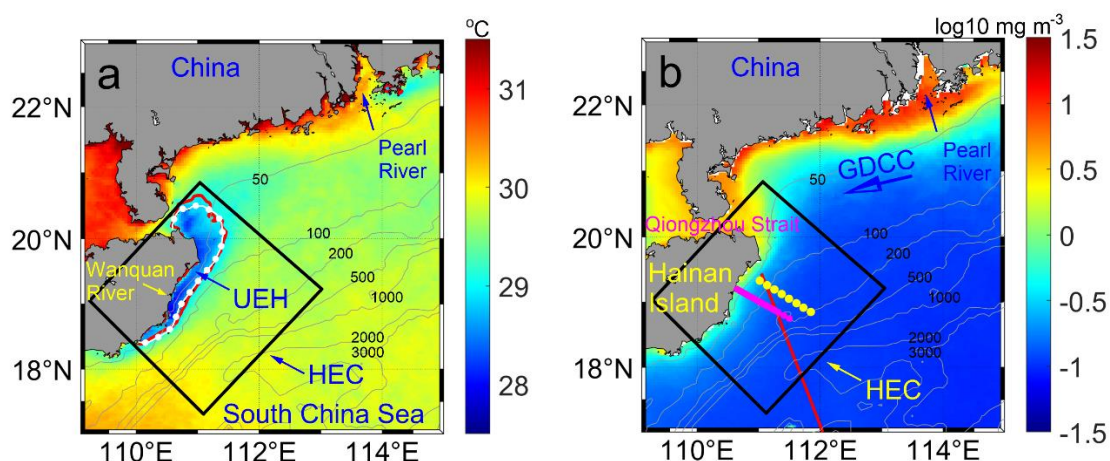
65   Figure 1. Study area (black solid square) and sampling sites. (a) Climatological (June-August) sea
66   surface temperature (SST) and (b) Chl-a concentration during 2003–2020. In panel (a), the white
67   dotted curve is the SST front for June-August; the red curve is the 29° isotherm. In (b), the dots
68   are the observation sites for the cruise during July 14–15, 2021 (yellow), and October 2–3, 2019
69   (magenta), and the red curve is the altimeter satellite ground track (Track 114). The unit of the
70   numbers on the isobaths is meters.

71

72   The variation in primary production in the HEC has been variously reported. Deng et al.
73   (1995) reported that phytoplankton achieved a maximum value in a strong period of UEH. Jing et
74   al. (2011) found a higher Chl-a concentration in summer 1998, as the offshore Ekman transport
75   was the strongest. Southwesterly monsoon-induced coastal upwelling is suggested to be the major
76   mechanism for the relatively high summertime phytoplankton biomass and primary production
77   (Liu et al., 2013; Song et al., 2012). Moreover, Hu et al. (2021) found that eddy processes could

78 strengthen phytoplankton blooms in the HEC. The variation in the basin circulation may also
79 affect the UEH (Su et al., 2013; Wang et al., 2006). However, Ning et al. (2004) reported poor
80 nutrients, low Chl-a, and weak primary production in summer in the HEC. Shi et al. (2021) found
81 that the largest Chl-a increase in the HEC occurs in May when upwelling is weak. Li et al. (2021a)
82 further showed that the maximum Chl-a concentration year-round exhibits a double peak in March
83 and October.

84   The results of previous studies indicate that upwelling may not be the most significant factor
85 affecting primary productivity in the HEC (Li et al., 2021a; Ning et al., 2004). The mechanism
86 driving the variation in primary productivity in the HEC thus needs further investigation.

87   The objective of this study is to reveal the role of upwelling in the spatial-temporal variations
88 in Chl-a concentrations in the HEC area based on multi-sensor satellite observations and in situ
89 cruise observations. The article is organized as follows. Section 2 describes the materials and
90 methods, including the algorithms used for retrieval of the total suspended sediment (TSS) and sea
91 surface temperature (SST) front from satellite observations. Section 3 presents the results and
92 variations in environmental factors, analysis of the spatial-temporal variations in the Chl-a
93 concentration in the study area. Section 4 discusses the role of typhoons, coastal currents, El Niño-
94 Southern Oscillation (ENSO) events, and precipitation in the Chl-a concentration. Section 5
95 presents the conclusions.

96

97 **2 Materials and methods**

98 2.1 Study area and upwelling area

99   The study area (enclosed by the black square in Figure 1) covers the UEH area off the
100 northeastern coast of Hainan Island. It is adjacent to the narrow Qiongzhou Strait in the west and
101 adjoins the wide continental shelf of the NWSCS in the east. The Wanquan River flowing through
102 east Hainan Island is the third largest river on Hainan Island. The East Asian monsoon prevails in
103 the HEC, and the UEH appears along the coast in summer (Lin et al., 2016). In fall and winter, a
104 southwestward current flows along the coast on the whole shelf (Ding et al., 2018; Li et al., 2016).
105 The nutrients in the Pearl River runoff can be transported to the HEC area by the Guangdong
106 Coastal Current (GDCC). The thermal fronts stretch along the continental shelf (dotted white
107 curve in Figure 1a) and are accompanied by relatively high Chl-a concentrations in HEC (Figure
108 1b).

109

110 2.2. Satellite observations and retrieval

111   The monthly ocean color elements (Kd490, Rrs645, Chl-a, SST, and photosynthetically
112 active radiation (PAR)) were obtained by moderate resolution imaging spectroradiometer
113 (MODIS) instruments onboard the Terra and Aqua satellites. The dataset from 2003 to 2020 is a
114 level-3 product with a spatial resolution of 4 km. The data from the two platforms were merged to
115 improve the coverage of the Chl-a concentration (Li et al., 2021b). The TSS concentration was
116 estimated from the Rrs645 product (Li et al., 2021b):

117
$$C_{\text{TSS}} = 0.6455 + 1455.7 \times Rrs645 \tag{1}$$

118   The euphotic depth retrieval from the Kd490 product was conducted as follows (Zhao et al.,
119 2013):

120
$$Z_{\text{eu}} = 0.28 + \frac{395.92 \times 0.0092}{0.0092 + Kd490} \tag{2}$$

The surface thermal front was estimated using the SST gradient. The SST gradient was calculated using the zonal and meridional components ($GSSTx$, $GSSTy$) as follows:

$$GSST = \sqrt{(GSSTx)^2 + (GSSTy)^2} \qquad (3)$$

where $GSSTx_i = \left(\frac{SST_{i+1} - SST_{i-1}}{x_{i+1} - x_{i-1}}\right)$ (°C/km), and ($x_{i+1} - x_{i-1}$) is equal to twice the spatial resolution.

The sea surface wind (SSW) at 10 m above the sea surface, with a spatial resolution of 0.25°, were obtained from the Copernicus Marine Service (CMEMS) (Hersbach et al., 2018). The wind data is a sub set from the fifth generation European Centre for Medium-Range Weather Forecasts (ECMWF) atmospheric reanalysis of the global climate covering the period from January 1950 to present. The data from 2002 to 2020 used in this study were a monthly product.

A cross-shelf and along-shelf coordinate system for the SSW vector is given by:

$$u_{\text{along}} = u\cos\theta - v\sin\theta \qquad (4)$$

$$v_{\text{cross}} = u\sin\theta + v\cos\theta \qquad (5)$$

where the cross-shelf wind, v_{cross}, is seaward positive; the along-shelf wind, u_{along}, is northward parallel to the coastline; θ is the angle between the shoreline and the north direction, 25° in this study; and (u, v) are the east and north components of the SSW.

The wind stress is determined as

$$\tau = \rho_a C_D U|U|$$

where ρ_a, C_D, and U are air density, drag coefficient and sea surface wind. $\rho_a = 1.29$ kg m^{-3}. $C_D = (0.75+0.067U) \times 10^{-3}$ (Garratt, 1977). Moreover, wind stress curl is obtained by $\nabla \times \tau$.

The monthly sea surface salinity (SSS) data from 2018 to 2020 with a spatial resolution of 0.25° were obtained from the CMEMS.

The daily rainfall rate during 2003–2020 was obtained from the multi-satellite precipitation analysis dataset of the Tropical Rainfall Measuring Mission (TRMM). The monthly data with a spatial resolution of 0.25° were calculated from the daily global rainfall data.

The satellite altimeter along-track sea level anomaly (SLA) data from 2003 to 2020 were obtained from the CMEMS. The Jason-1, Jason-2, and Jason-3 satellites repeat their ground tracks every 9.9 d. Their sampling frequency is 1 Hz, and their spatial resolution is approximately 7 km. The 5-point moving average was applied to the along-track SLA data to filter out the small-scale ocean processes. As the coastline is almost perpendicular to ground track 114 of the altimeter satellites (Figure 1b), the along-shelf geostrophic current was estimated from the along-track SLA data as follows:

$$u = \frac{g}{f}\frac{\partial \eta}{\partial y}, \qquad (6)$$

where g is the acceleration due to gravity, f is the Coriolis parameter, and η is the SLA.

The typhoon track data were downloaded from the Tropical Cyclone Data Center of the China Meteorological Administration (CMA). The dataset contains 6-hourly tracks and intensity analyses of typhoons that occurred in the western North Pacific from 2003 to 2020.

2.3. Shipboard sections

Two shipboard sections were investigated during October 2–3, 2019, and July 14–15, 2021 (red and magenta points in Figure 1b). At each station, the temperature, salinity, and fluorescence

profiles were collected using a Sea-Bird 911plus conductivity-temperature-depth (CTD) system. The Chl-a data from the fluorescence sensor of the CTD were not calibrated, and the signals of interest were clear.

2.4. Mapping the upwelling

The thermal fronts (Figure 1a) of the climatological SST in the summer stretched along the 29°C isotherm. Thus, we defined the upwelling domain, i.e., core upwelling, as the area where the SST was lower than 29°C in the summer. The time series of the core upwelling area was calculated for each year during 2003–2020. Then, the time series of the Chl-a concentration in the core upwelling area for each year was obtained.

The upwelling index (UI) based on the wind stress is as follows:

$$M_x = -\frac{\tau_y}{f\rho}, \tag{7}$$

where $\rho = 1025$ kg m^{-3} is the water density, f is the Coriolis parameter, τ_y is the along-shelf wind stress, and M_x is the cross-transport.

2.5. Empirical orthogonal function

Empirical orthogonal function (EOF) is a useful tool and widely applied to reduce the dimensionality of climate data (North et al., 1982). EOF analysis is used to determine the dominant patterns of Chl-a in the study area. The Chl-a data is prepared as an anomaly in the form of matrix, X. Decomposition is applied by B·E = X. EOF modes (i.e., E, spatial patterns) and their corresponding principal components (i.e., B, temporal coefficients) could be obtained by decomposition of the anomaly matrix. The EOF patterns and the principal components are independent.

3 Results

3.1 Temporal and spatial variations environmental factors in the HEC

Figure 2 shows the climatological monthly variations in the environmental factors in the study area. As shown in Figure 2a, the mean along-shelf component of the SSW is positive from May to September, with the strongest value of 2.5 m s^{-1} occurring in June. In the rest of the months, the along-shelf components of the SSW and wind stress curl are negative. The cross-shelf component of the SSW is also negative. The changes in the wind direction show that the study area is mainly controlled by the Asian monsoon. The period of UEH is coherent with that of the positive along-shelf wind and the wind stress curl from May to September (green shading in Figures 2a–d), indicating the effects of SSW and wind stress curl on coastal upwelling.
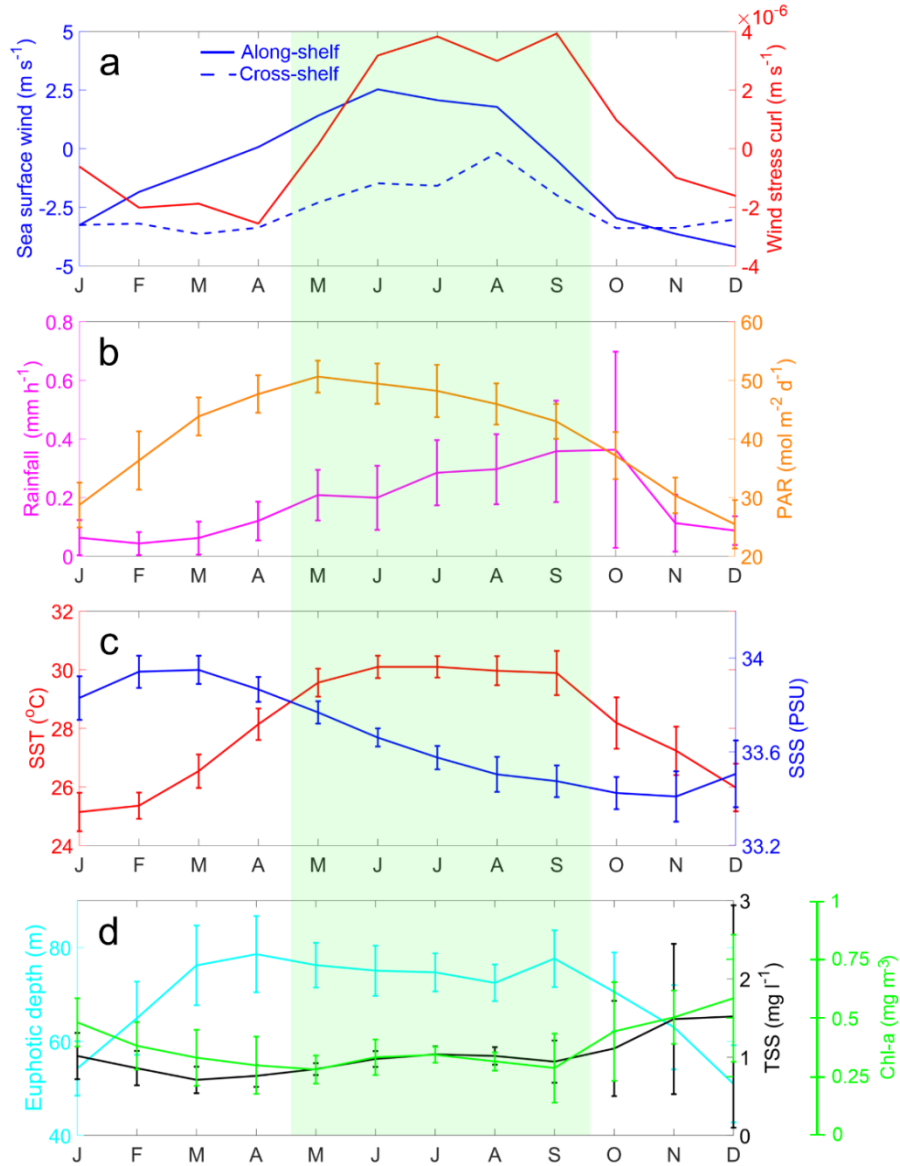
198   Figure 2. Monthly climatological (a) sea surface wind and wind stress curl, (b) rainfall and PAR,

199   (c) SST and SSS, and (d) euphotic depth, Chl-a and TSS in the study area. The error bar indicates

200   the standard deviation (STD). The shaded area indicates the upwelling season.

201

202   The rainfall in the study area increases monotonically from February to October and peaks in

203   October with a value of 0.37 mm h^{-1} (Figure 2b). After October, the rainfall decreases rapidly to

204   0.10 mm h^{-1} in November. The rainfall in winter (December, January, and February) was less than

205   0.10 mm h^{-1}. Different from the rainfall, the mean photosynthetically active radiation (PAR) in the

206   study area reaches its maximum value of 50 mol m^{-2} d^{-1} in May, indicating its dependence on the

207   annual movement of the sun. The monthly climatological distribution of the SST is similar to that

208   of the PAR, while the highest (lowest) SSS occurred in March (October and November) following

209   the amount of rainfall (Figure 2c).

210   For the euphotic depth, the average values in the study area are greater than 50 m all year

211   around and reach 70 m in the months of March to October (Figure 2d). In contrast, the TSS

212   concentration is less than 1.0 mg l^{-1} from January to September and reaches the highest value of

213   1.5 g l^{-1} in December. Similar to the TSS, the mean Chl-a concentration in the study area has

214 smaller values of less than 0.3 mg m^{-3} from March to September, although the UEH occurs in the
215 summer months (green shading in Figure 2).
216   Figure 3 shows the spatial distributions of seasonal climatological environmental parameters.
217 The PAR is almost homogeneous in the study area (Figure 3a). The values are approximately 20–
218 30 mol m^{-2} d^{-1} in winter, reach 50 mol m^{-2} d^{-1} in the spring and summer, and then decrease to
219 approximately 30–40 mol m^{-2} d^{-1} in autumn.
220

221
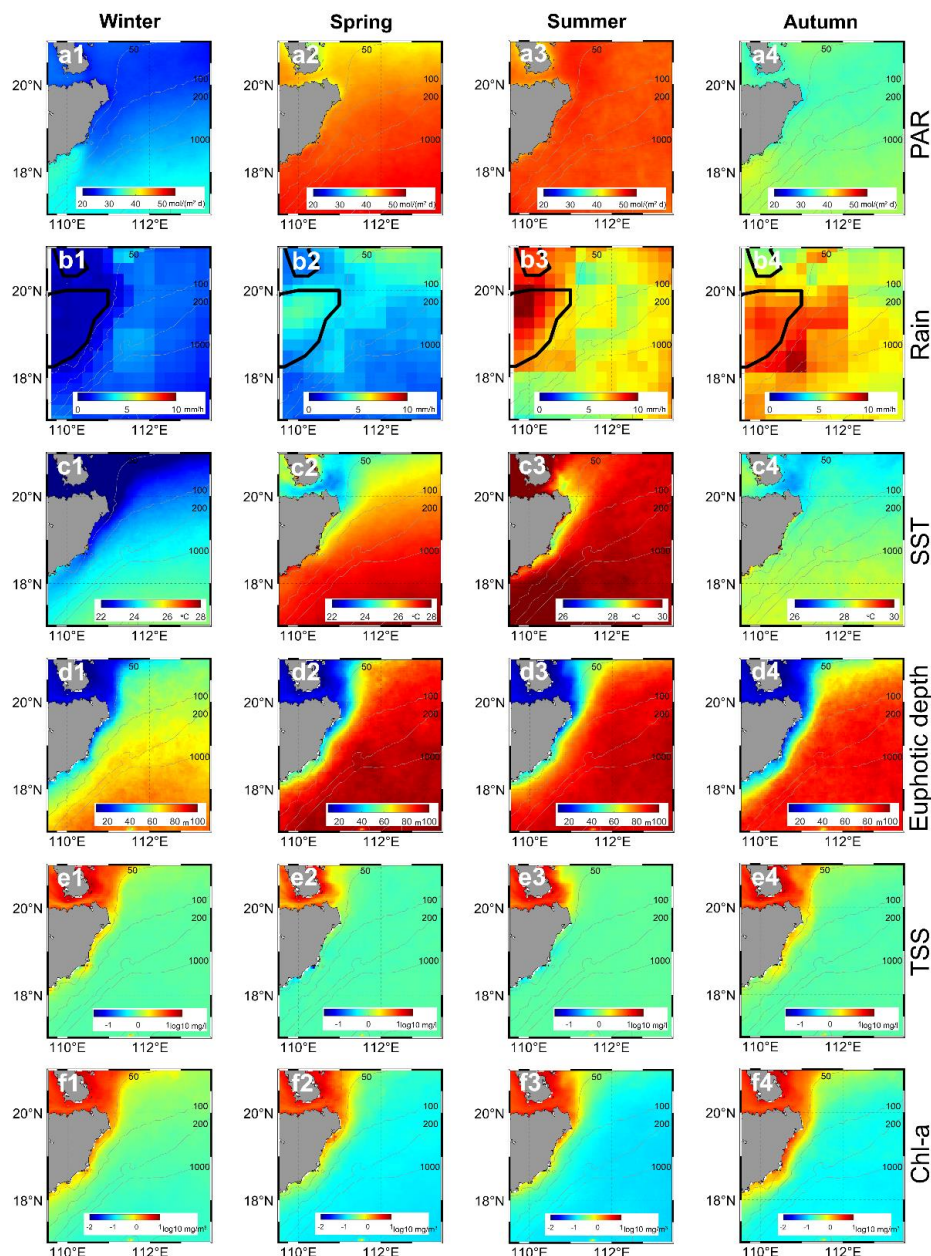
222 Figure 3. Seasonal climatological (a1–a4) PAR, (b1–b4) rainfall, (c1–c4) SST, (d1–d4) euphotic
223 depth, (e1–e4) TSS, and (f1–f4) Chl-a. The columns correspond to winter, spring, summer and
224 autumn. The unit of the numbers on the isobaths is meters.

225

226   The rainfall rate is less than 5 mm h^{-1} in winter (Figure 3b). In spring and summer, the
227 rainfall peaks in Hainan Island, while the high precipitation area is located on Hainan Island and

in the HEC area in autumn. The rainfall rate is as high as 10 mm h^{-1} in summer and autumn. Furthermore, as the high precipitation area is located on land, the heavy rain is transformed into runoff, which carries nutrients into the sea. Thus, the temporal and spatial variations in the rainfall rate likely induce variations in the input of terrestrial materials.

The SST exhibits remarkable seasonal variability (Figure 3c). Generally, the SST is high in spring and summer and low in winter and autumn. Moreover, the SST is lower in coastal waters than in ocean areas in winter and spring, which is modulated by the prevailing southwestward current along the coastline of Guangdong (Ding et al., 2018). In summer, a region identified by low SST (<29°C) values, i.e., the UEH, is observed to the northeast of Hainan Island.

The spatial distribution of the euphotic depth is consistent with the bathymetric distribution (Figure 3d). The euphotic depth in spring and summer is approximately 20–30 m within water depths of less than 50 m, whereas it is approximately 100 m in the deeper water. In winter and autumn, the euphotic depth is 20–30 m within water depths of less than 70 m. Moreover, the euphotic depth decreases to 60–80 m in the deeper water. As the latitude of the study area is low, the illumination is not the limiting factor. These variations in the euphotic depth likely affect the vertical distribution of phytoplankton in the water.

Similarly, the TSS concentration is higher in the coastal area and lower in the ocean area (Figure 3e). Moreover, the TSS concentration is less than 0.3 mg l^{-1} in spring and summer in the HEC area. However, the TSS concentration increases to 3.0 mg l^{-1} at water depths of less than 70 m in autumn and winter.

The Chl-a concentration is higher in the coastal area than in the open ocean area (Figure 3f). In winter and autumn, the Chl-a concentration is higher than 1.0 mg m^{-3} at water depths of less than 70 m. In spring, the Chl-a concentration decreases to 0.5 mg m^{-3}. However, the Chl-a concentration decreases to approximately 0.3 mg m^{-3} in summer. In addition, the high concentration is approximately 1.0 mg m^{-3} in the nearshore area with water depths of less than 20 m.

3.2. Variabilities in upwelling

The UI derived from the wind stress and wind stress curl in the HEC are shown in Figure 4. The results reveal that the UI decreased from 2003 to 2013 and increased from 2014 to 2020, probably due to the phase switching of the Pacific Decadal Oscillation (PDO) in 2014 (Qin et al., 2018). Overall, the UI from wind stress exhibited an increasing trend from 2003 to 2020. Moreover, the wind stress curl exhibited a weak increasing trend from 2003 to 2020. Because the period of data is only 18 years, it is a little too short to demonstrate the significance of the trend. Therefore, p value and r are not so statistically significant owing to the limitation of data.

264
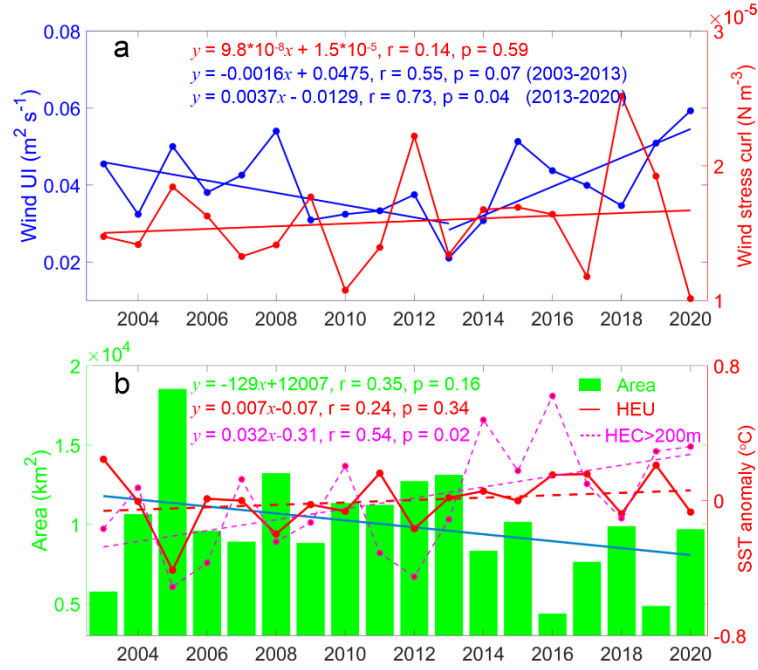
Figure 4. Time series of Upwelling index (UI) and upwelling characteristics. (a) Time series of mean sea surface wind UI and wind stress curl in HEC region. Blue dotted curve denotes the mean UI during June-August; the red dotted curve is mean wind stress curl during June-August; and blue and red curves are the trends of the UI and wind stress curl, respectively. (b) Time series of upwelling area and SST. Green bar denotes the area of UEH region. Red and magenta dotted curve denote mean SST of UEH region and slope region (depth>200 m) in HEC, respectively. Blue, red and magenta curves are the trends of the upwelling area, mean SST in UEH and slope area, respectively.

The area and SST of the UEH are shown in Figure 4b. The time series of the area of UEH exhibited a downward trend from 2003 to 2020. Moreover, the mean SST in the UEH exhibited an increasing trend. The trends of both the area (-129 km^2 y^{-1}) and mean SST (0.007°C y^{-1}) indicate that the UEH gradually weakened from 2003 to 2020. However, we checked the mean SST of background (>200 m in HEC, magenta curve in Figure 4b). It shows that the SST of background increases much faster than that in UEH. Therefore, we conclude that the upwelling is enhanced by the stronger wind stress and curl, under the background of SST becoming stronger.

The time series of the UEH area and UI exhibit interannual variations. High UI and wind stress curl values occurred in 2005, 2008, 2012, 2015, and 2018, which coincided with the large areas of upwelling in these years. Low UI values occurred in 2004, 2006, 2009, 2016 and 2019, which coincided with the small areas of upwelling in these years.

3.3. Variabilities in Chl-a concentration in the UEH

The time series of the spatial mean of the Chl-a concentration in the UEH is shown in Figure 5. The Chl-a concentration is unexpectedly low from April to September, i.e., the upwelling season (as shown in Figures 5a-b). The climatological mean Chl-a concentration is the lowest in summer, 0.74 mg m^{-3} (as shown in Figure 5b and Table 1), which indicates the relatively limited effect of upwelling on the Chl-a concentration in the HEC. However, the mean Chl-a

concentration in the UEH is highest in autumn (1.18 mg m^{-3}) and almost twice as high as that in summer. In October, the mean Chl-a concentration is as high as 1.4 mg m^{-3}.
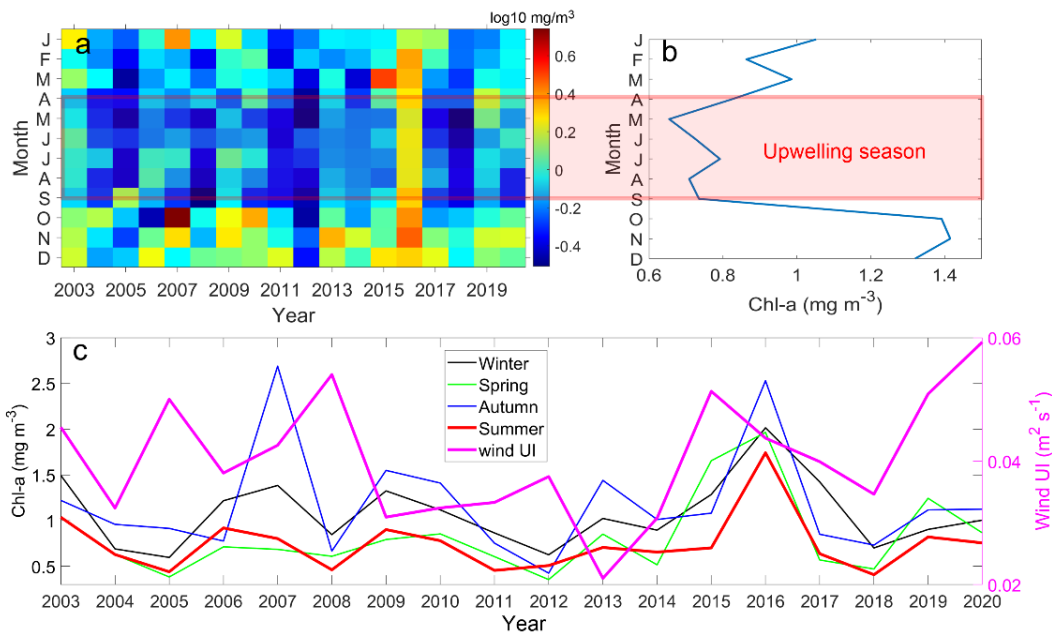
Figure 5. Time series of (a) the spatial mean of the Chl-a concentration in the upwelling area, (b) the monthly climatological mean Chl-a, (c) the seasonal mean Chl-a and wind UI. The red shading indicates the upwelling season from April to September.

Table 1. Seasonal climatological mean Chl-a concentration in the UEH.

Period	Winter	Spring	Summer	Autumn	Annual mean
Value	1.08 ± 0.24	0.82 ± 0.44	0.74 ± 0.06	1.18 ± 0.23	0.96 ± 0.27

The interannual variations in the spatial mean of the Chl-a concentration in the UEH are also shown in Figure 5. The Chl-a concentration in the UEH was high in 2003, 2006–2007, 2009–2010, 2013, 2015-2016 and 2019. The Chl-a concentrations in these years were 2–4 times (ranging from 1.0 to 1.8 mg m^{-3}) those in the other years (2005, 2008, 2011-2012 and 2018). In the remaining years, the Chl-a concentration is only approximately 0.5 mg m^{-3} in summer, which is much less than the mean value. In 2018, there were minima for both of wind UI and Chl-a. However, the maximum of wind stress curl existed in 2018, which means the strongest wind stress curl was the leading factor for the upwelling process (as show in Figure 4a).

Comparing the time series of Chl-a concentration shown in Figure 5 to the time series of upwelling characteristics, one can see that low UI values coincide with high Chl-a concentration in the UEH, and vice versa. The correlation coefficient between wind UI and Chl-a concentration during 2003-2012 is -0.3, which shows a negative relationship. It is known that low UI values indicate weak upwelling in the HEC. This means that upwelling is a limiting factor in the UEH. Moreover, one can see that the Chl-a concentration is unexpectedly low in the upwelling season, as shown in Figures 5. Therefore, the results provide new insight into the relationship between marine productivity and upwelling in the UEH. However, the effect of environmental factors and spatial variations on the Chl-a concentration need further investigation.

320 3.4 EOF analysis of Chl-a concentration

321   To further reveal the variations in the Chl-a concentration in the HEC, the empirical
322 orthogonal function (EOF) analysis results are shown in Figures 6–7. The first four EOF modes of
323 the Chl-a concentration explain 60% of the total variance (Figure 6). Mode 1 includes an enhanced
324 signal in the coastal waters (<60 m) to the east of Hainan Island. The magnitude of the variability
325 is generally the same throughout the other areas. The corresponding temporal evolution (Figure
326 7a) is characterized by strong seasonal cycles, with peaks in October and troughs in May. The
327 climatological mean of the corresponding temporal evolution is negative from April to September
328 and positive from October to March. The negative phase with a large amplitude lasts for six
329 months. Therefore, the Chl-a concentration is persistently low from April to September. Mode 1 is
330 characterized by the GDCC (Ding et al., 2018). Mode 2 separates the east and northeast coastal
331 waters of Hainan Island. The troughs of the temporal evolution of Mode 2 occur in September and
332 October. The climatological mean peaks in January and December. The strong signals occur in
333 September and October to the east of Hainan Island, which indicates that the Chl-a concentration
334 is controlled by rainfall (as shown in Figure 3b). The other strong signals occur in January and
335 December. Moreover, they are located on the north shelf of the SCS, adjacent to the Qiongzhou
336 Strait to the west. Thus, the result suggests that Chl-a concentration is affected by the GDCC.

337
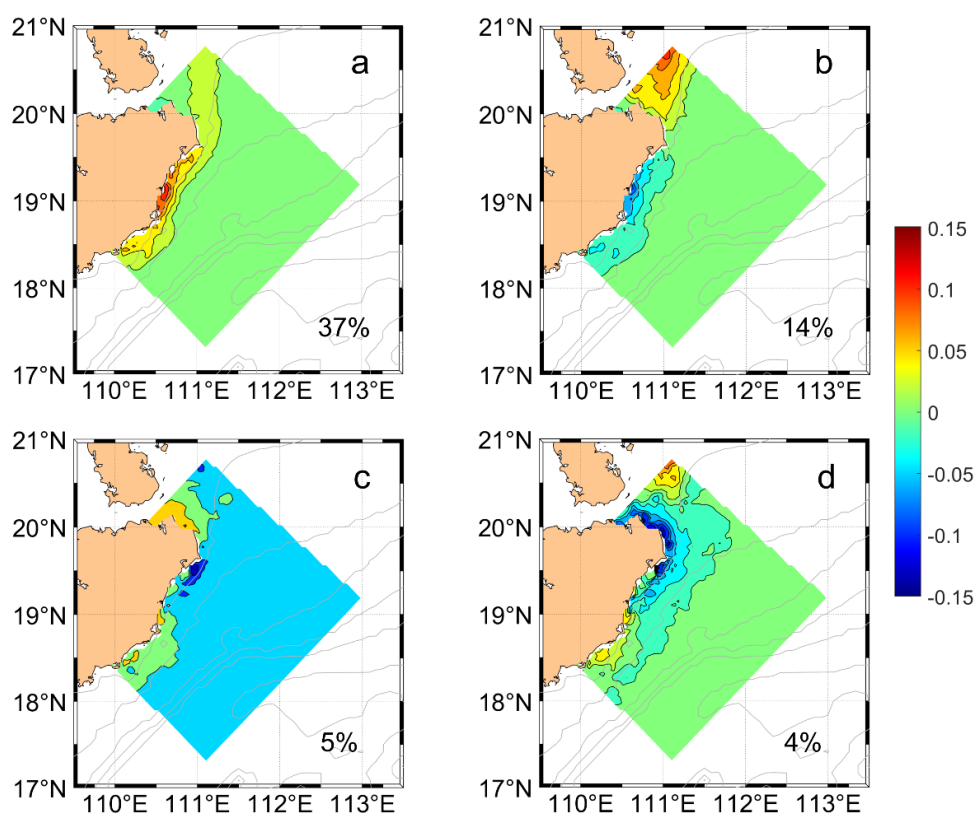
339 Figure 6. Spatial distributions of the first four EOFs for the Chl-a concentration. The variance
340 explained by each mode is labeled.

341

342
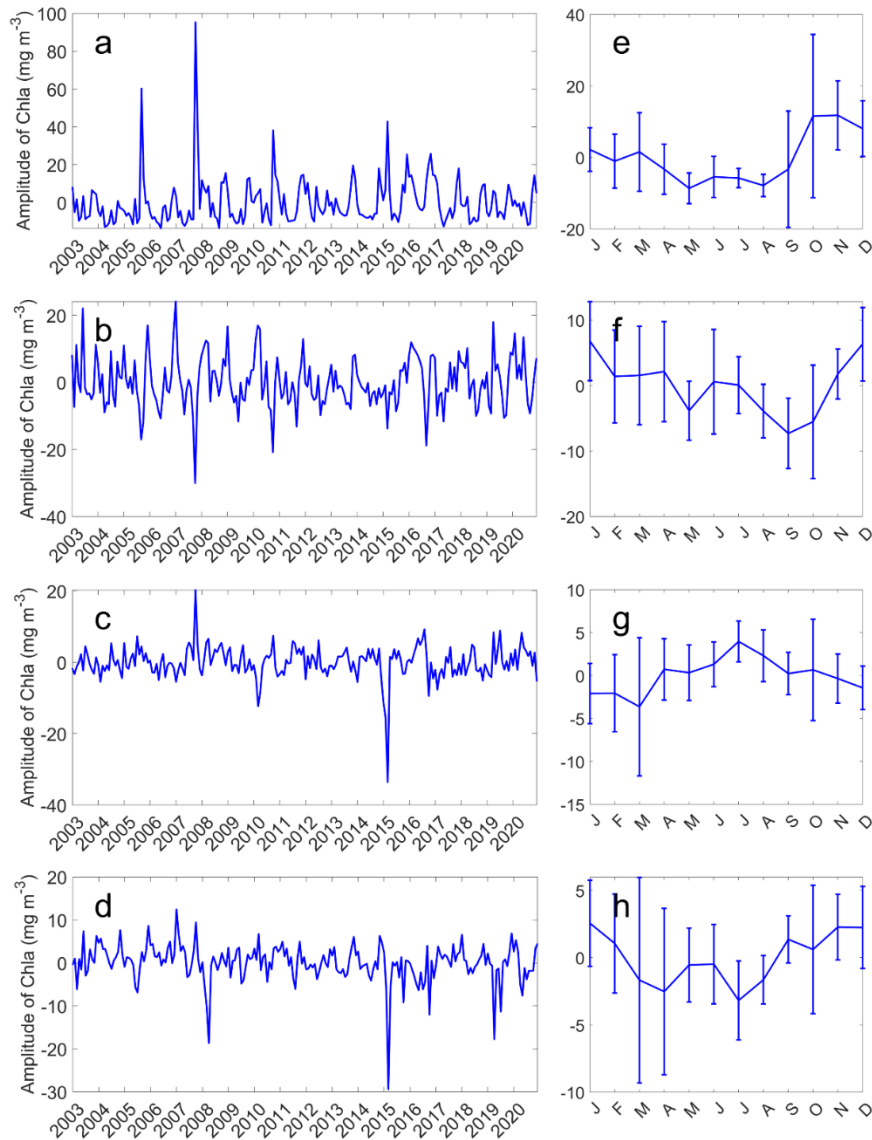
343   Figure 7. (a–d) Time series and (e–h) climatological mean of the first four EOFs for the Chl-a

344   concentration.

345

346   Mode 3 describes 5% of the total variance in the Chl-a concentration in the coastal regions of

347   Hainan Island. Mode 3 also separates the east and northeast coastal waters of Hainan Island

348   (Figure 6c). However, the climatological mean of the temporal evolution is positive between June

349   and August. Therefore, the positive phase occurs in summer, revealing an upwelling area to the

350   east and north of Hainan Island. Mode 4 contributes only 4% of the total variance. The

351   climatological mean of the temporal evolution exhibits strong peaks in July and weak peaks in

352   April, i.e., semiannual variability. High Chl-a concentrations occur in the northeast coastal water

353   of Hainan Island during the upwelling season.

354   Modes 3 and 4 both describe the upwelling phenomenon along the northeast coast of Hainan

355   Island during summer. The spread of upwelling can be seen clearly in the EOFs of the Chl-a

356   concentration in the areas with water depths of less than 100 m along the coastline. However,

357   upwelling described less than 10% of the total variance in the Chl-a concentration, indicating that

358   the contribution of upwelling to productivity in the HEC is limited.

359

3.5 Vertical distribution of the Chl-a concentration based on observation data

To examine the vertical distribution of the Chl-a concentration in the HEC, two cruise measurement sections are used in this study. Figure 8 shows the oceanographic cruise data collected on July 14–15, 2021, and October 2–3, 2019, illustrating the distribution of the Chl-a concentration in summer and autumn, respectively. The pronounced upwelling can be seen on the cross-shelf section observed in July 2021. Both the isotherm and isohaline on the shelf are uplifted toward the shore by upwelling-induced movement. A temperature front can be seen near the sea surface, which is located approximately 50 km away from the coastline (depths of ~90 m). The thermal fronts are reported by Jing et al. (2016). The fronts induced by upwelling tend to be approximately aligned with the 20–100 m isobath. The high Chl-a concentration layer is also uplifted from 80 m to 40 m by upwelling, and the Chl-a concentration is as high as 1.2 mg m^{-3}.

371

372
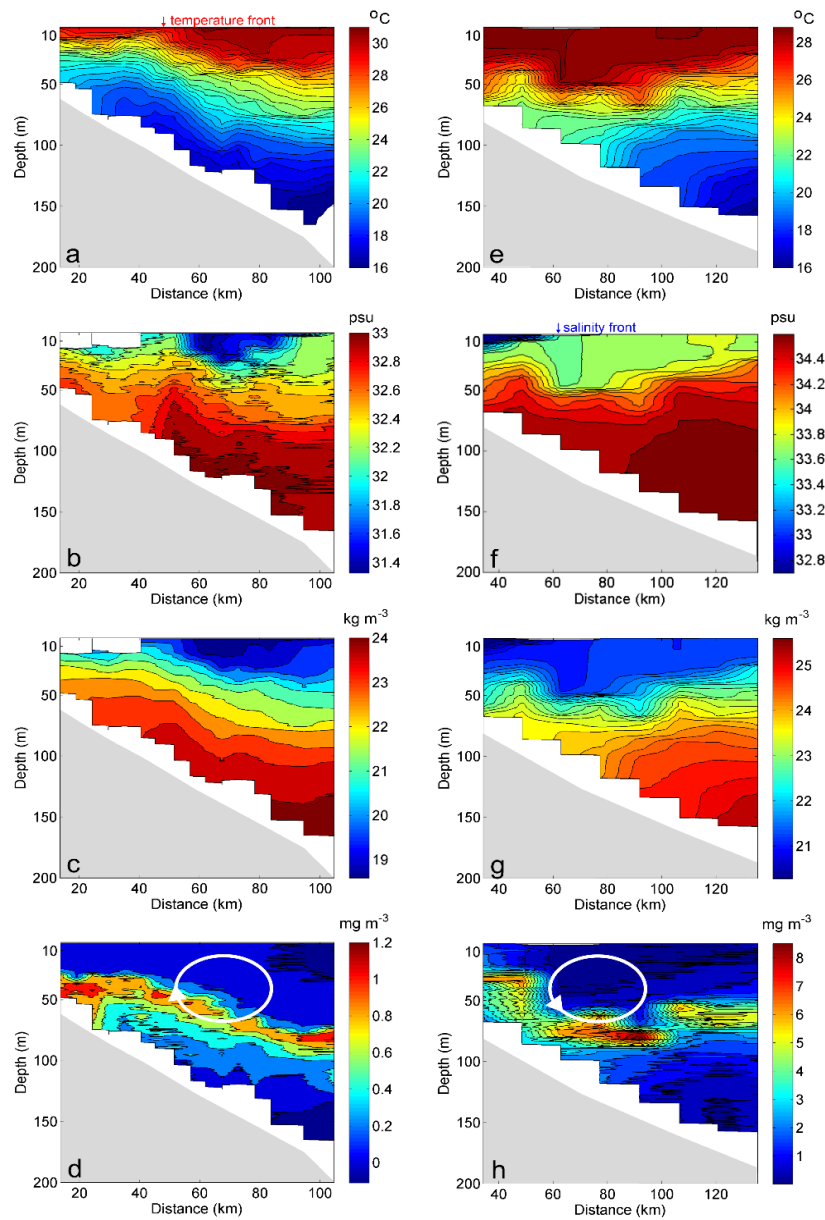
Figure 8. Oceanographic cruise data collected on (a–d) July 14–15, 2021, and (e–h) October 2–3,

2019: a) and e) temperature distributions; b) and f) salinity distributions; c) and g) potential density distributions; and d) and h) Chl-a distributions. The arrows indicate location of the temperature and salinity front near the sea surface. The white circle is a diagrammatic sketch for upwelling and downwelling circulation.

From October 2–3, 2019, the sea surface temperature front disappeared. Jing et al. (2016) found that the front was the weakest in autumn. However, a salinity front occurs approximately 60 km from the coastline in the sea surface. This salinity front indicates that fresh water is injected into the sea surface. Figures 2b and 3b4 show that the rainfall is strong during autumn. The rainfall is input into the sea surface via rainfall and runoff. Thus, the salinity front is generated. In contrast to the upwelling in summer, downwelling occurs in the bottom water and is associated with downwelling-favorable wind forcing. Moreover, abundant Chl-a is detected at a depth of 30 m on the shelf, which is shallower than the detection depth in summer since the euphotic depth is shallower in autumn, as shown in Figure 3d.

4 Discussion

4.1 Relationship with typhoon events

In the NWSCS, the Chl-a concentration can be affected by different factors, e.g., typhoons. Typhoon-induced upwelling occasionally occurs in the SCS (Ma et al., 2021; Wang et al., 2020). In the shelf areas, typhoon-enhanced vertical mixing and upwelling play dominant roles in the spatiotemporal behavior of the Chl-a concentration (Li et al., 2021a; Li et al., 2021b). The upwelling transports nutrients into the euphotic zone, which supports Chl-a blooms (Ye et al., 2013; Zheng et al., 2021). An increase in the Chl-a concentration in the nearshore region off Hainan Island followed typhoon rainfall, with mixing and upwelling effects (Zheng and Tang, 2007). The large-scale peripheral wind vector resulted in the accumulation and enhancement of the Chl-a concentration in the nearshore area (Liu et al., 2020). An offshore bloom produced a Chl-a peak (4 mg m^{-3}) after the typhoon's passage (Zheng and Tang, 2007). These observations illustrate the effects of typhoons on the marine ecosystem in the HEC.

Figure 9 shows the time series of the number of typhoons that passed over the HEC during 2003–2020. Sixty-eight typhoons passed across the continental shelf of the NWSCS during this 18-year period. There were interannual variations in the time series of the number of typhoons. As many as nine typhoons were generated and affected Qiongdong in 2013, while fewer than two typhoons passed by the study area in 2004, 2007, 2010, and 2014–2015. Seasonally, 33 typhoons passed by in summer and autumn. As shown in Figure 5b, a small peak in the mean Chl-a concentration occurred in July. Moreover, the Chl-a concentration was high in 2013, especially in autumn, varied within the range of 0.7–1.5 mg m^{-3}, and coincided with the occurrences of nine typhoons. This indicates that the high Chl-a concentrations were related to the typhoons. However, typhoons occur on the synoptic scale and influence the coastal area for several days. Therefore, these processes seem to have a limited effect on the monthly mean Chl-a concentration.
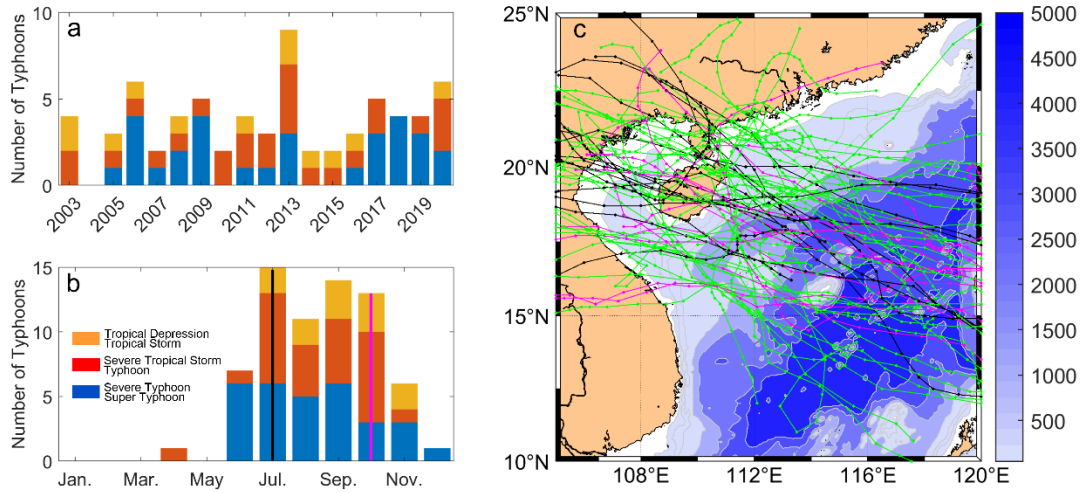
Figure 9. (a) Time series of the number of typhoons that passed by the study area during 2003–2020. (b) Seasonal distribution of typhoons. (c) Trajectories of typhoons during 2003–2020. The orange, red, and blue bars in (a–b) represent the numbers of tropical depressions and tropical storms, severe tropical storms and typhoons, and severe typhoons and super typhoons, respectively. The magenta and black curves in (c) represent the typhoons that passed by the study area in July and October, respectively. The green curves represent the typhoons that passed by the study area in the other months.

4.2 Role of the coastal current

The current in the NWSCS contributes significantly to the transport of low-salinity water, nutrients, and phytoplankton, and it also affects the ecological environment (Ding et al., 2018; Meng et al., 2017). The shelf circulation pattern is dominated by monsoons, tides, buoyancy forcing, and topography. Due to the changes in the wind direction, the current direction changes in the different seasons. In autumn and winter, the current in the NWSCS is predominantly southwestward. It changes northeastward in summer (Ding et al., 2018). The monsoon plays an important role in the current, which induces onshore and offshore Ekman transport on the shelf during the winter and summer monsoons, respectively. Gan et al. (2013) found that transport was induced by amplified geostrophic transport during downwelling events. Here, we used geostrophic current retrieval from along-track satellite altimeter data on the shelf of the NWSCS to reflect the role of the coastal current on the Chl-a concentration.

The latitudinal distribution of the climatological along-track SLA is shown in Figure 10. The climatological sea surface in the shelf side is higher than that in the ocean side in October, November, and December. And, the sea surface on the shelf was lower than that in the ocean from April to August. The geostrophic current shows that the current was positive (northeastward) between April and August, and it was negative (southwestward) between October and March. The climatological geostrophic current in September was approximately 0 m s^{-1}, which indicates that the current direction changed frequently. The climatological geostrophic current was stronger than 0.1 m s^{-1} in summer, and it was strongest in October, at approximately 0.17 m s^{-1}.
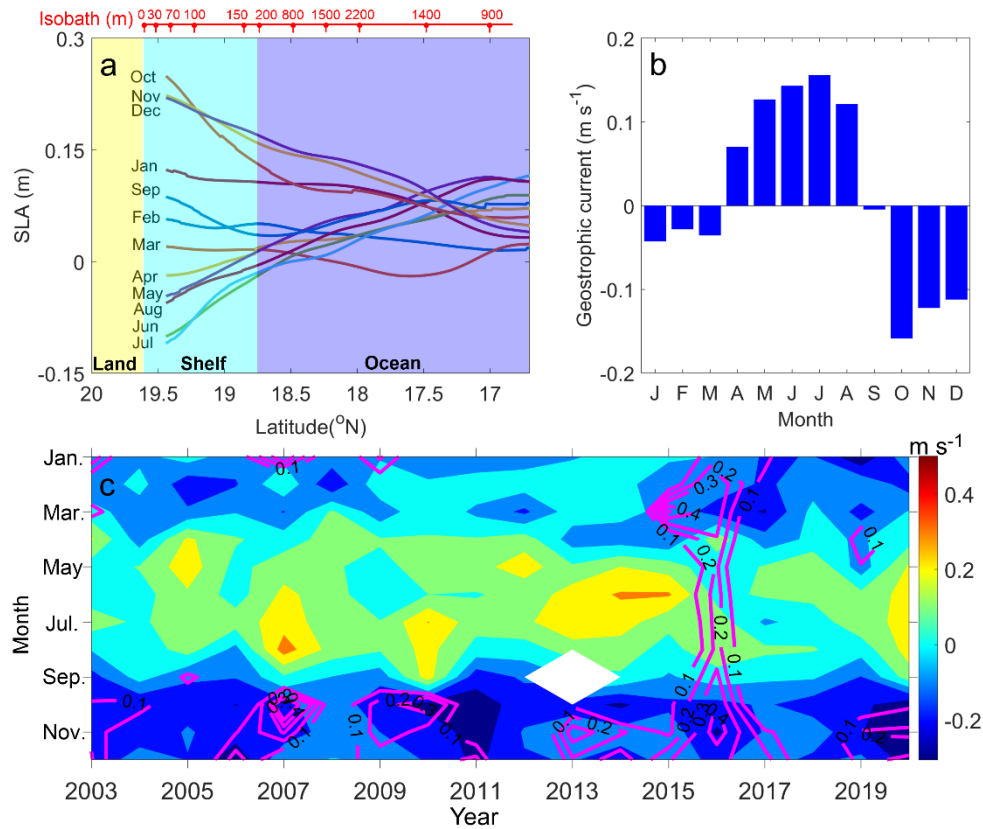
Figure 10. (a) Latitudinal distribution of climatological along-track SLA (track number: 114). (b) Geostrophic current retrieval from climatological along-track SLA. (c) Time series of geostrophic current (contours) and Chl-a concentration (magenta contour curves). The blue, cyan, and yellow shading in (a) represent the ocean, continental shelf, and land areas, respectively. The red bar with numbers in (a) indicates the water depth of the along-track SLA data. The values in (c) are the exponents of the Chl-a concentration.

In autumn and winter, the abundant nutrients in the GDCC, which were provided by the Pearl River, likely supported the high food availability to the phytoplankton (Yang and Ye, 2022). The GDCC was characterized by a high TSS (Figure 2d and 3e). TSS is synergistic with the concentration of dissolved nitrogen and is the dominant factor affecting the Chl-a concentration (López Abbate et al., 2017). The distribution of the monthly climatological Chl-a concentration (Figure 5b) was similar to that of the geostrophic current. In summer, the Chl-a concentration was low during the northeast oligotrophic current. In winter, the Chl-a concentration was high during the southwest nutrient-rich current. Figure 10c presents the time series of the geostrophic current and Chl-a concentration. The negative current and high Chl-a concentrations mainly occurred in autumn and winter, which demonstrates the crucial role of the current.

4.3 Role of rainfall

The phytoplankton responded more positively to the increased precipitation in the coastal waters (Thompson et al., 2015). Kim et al. (2014) reported that the increase in wind speed accompanied by rainfall was a major contributor to the Chl-a concentration. The precipitation directly deposits the nutrients in the air into the seawater. In addition, most of the rainfall on land runs over the land surface into the rivers and eventually into the ocean, transporting nutrients to

the ocean. Therefore, rain plays an important role in the variability of phytoplankton in coastal waters.

Figure 11 shows the time series of the monthly mean rainfall rate and Chl-a concentration. The rainfall rate was high in the summer and autumn, ranging from 0.3 to 1.4 mm h^{-1}. In October in 2007–2017, the monthly mean rainfall rate (>0.5 mm h^{-1}) coincided with the high Chl-a concentration.
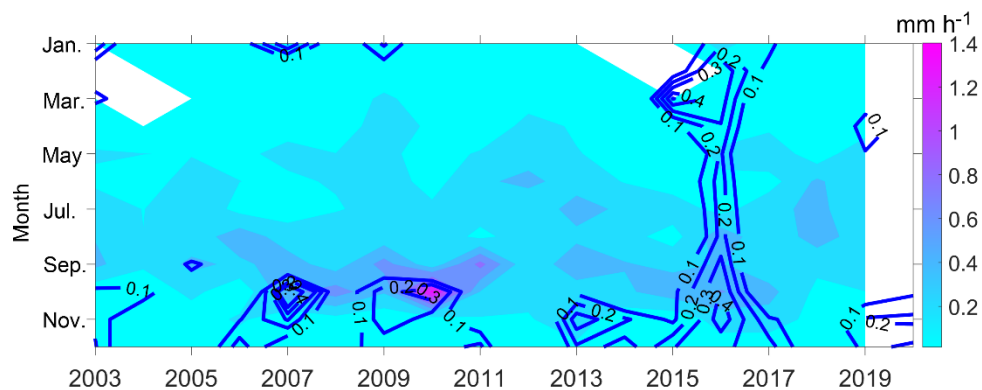
Figure 11. Time series of the rainfall rate (contours) and Chl-a concentration (blue curves with text labels). The values on the contours are the exponents of the Chl-a concentration.

Runoff is the main source of silicate in coastal waters (Zhang et al., 2003). Chen et al. (2016) observed that the concentration of silicate was as high as 2–12 μmol l^{-1} in the coastal waters of the HEC and had a positive correlation with the Chl-a concentration. Wang et al. (2018) found that diatoms contributed 88.11% and 85.81% of the total phytoplankton abundance in the northern SCS in May and October, respectively. The Chl-a concentration can increase by 0.3 mg·m^{-3} after a rainfall event (Zeng et al., 2022). Moreover, in Mode 2 of the EOFs (Figures 6–7), the positive phase of the Chl-a concentration occurred off the east coast of Hainan Island in October, which is near the estuary of the Wanquan River. Therefore, the runoff caused by the high rainfall rate triggered the high Chl-a concentrations in the HEC.

4.4 Relationship with ENSO events

ENSO has an indirect positive effect on the Chl-a concentration through its influences on precipitation, winds, SST, and turbidity (López Abbate et al., 2017). In the SCS, easterly wind anomalies and SST warming occurred in the summer following El Niño events (Yang et al., 2015). During El Niño events, the weakened southwesterly monsoon suppresses ocean upwelling (Jing et al., 2011; Kuo et al., 2008). The reverse occurs during La Niña events. Jing et al. (2011) found that the significantly strengthened wind stress of the 1998 summer induced strong upwelling, and the Chl-a concentration was much higher than in any of the other years. Yu et al. (2020) showed that the interannual variability indicates low levels of Chl-a southeast of Vietnam during El Nino years because of the weakened southwest monsoon. These previous studies conclude that the weaking sea surface wind appears in El Nino years.

In the upwelling season, i.e., summer, the wind stress was smaller during El Niño events (Table 2) than during La Niña events (Figure 4a). The Chl-a concentration in July during El Niño events increased to as high as 1.0 mg m^{-3} (higher than magenta dashed line in Figure 12).

Moreover, the SST of the core upwelling area was higher, but the core area was smaller (Figure 4b). After La Niña events, the Chl-a concentration is anomaly low (pointed out by cyan arrows). There are some exceptions, i.e., during 2015-2016. The wind stress and curl were both strong during 2015-2016. The eastern-Pacific (EP) type of El Niño causes the stronger wind anomaly, then the Chl-a concentration is higher than that in the Central-Pacific type (Yu et al., 2012).Jing et al. (2011) have reported anomaly high Chl-a concentration in another EP El Niño event. Therefore, ENSO events regulated the Chl-a concentration of the upwelling through wind stress. Huynh et al. (2020) have point out that the Chl-a variability in the SCS is influenced by the ENSO with a time lag of 4–9 months. Further research is required to investigate the relationship between the Chl-a variability and ENSO in the HEC.
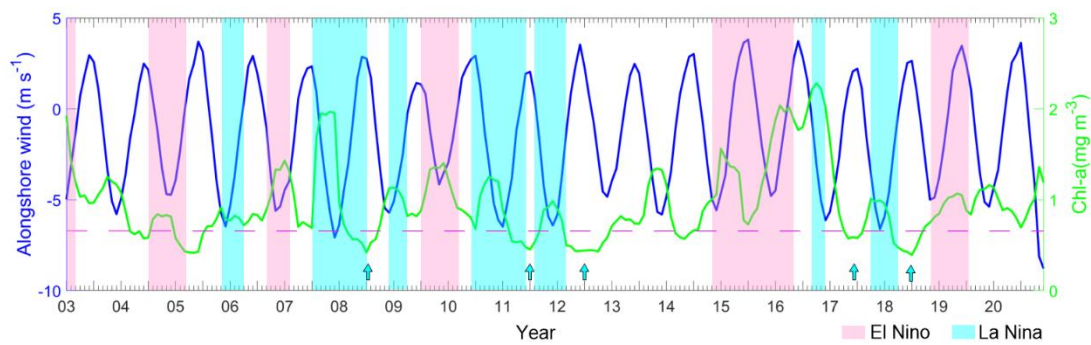
Figure 12. Time series of Chl-a (green curve) and along-shelf wind (blue curve). Stripes point out the El Nino (magenta) and La Nina (blue) events. Cyan arrows point out the minima value of Chl-a concentration. Magenta dashed line indicate high Chl-a concentration during El Nino events.

Table 2. ENSO events during 2003–2020.

ENSO event	Years (pattern)
El Niño	2002-2003(CP), 2004-2005(CP), 2006-2007(EP), 2009-2010(CP), 2015-2016(EP), 2018-2019(CP)
La Niña	2005-2006, 2007–2008, 2008-2009, 2010–2012, 2016, 2017–2018

CP: Central-Pacific; EP: Eastern-Pacific

In autumn, especially October, the spatial mean Chl-a concentration in the upwelling area was as high as 1.18 ± 0.23 mg m^{-3}. The precipitation was heavier during La Niña events (i.e., in 2005, 2007, 2010–2011, and 2016) than during El Niño events. Furthermore, the along-shelf current from the north was crucially important to the Chl-a concentration. There was a positive relationship between the Chl-a anomalies and the La Niña events.

4.5 Mechanisms of Chl-a variations in the HEC area

Figure 13 shows the relationships between the geostrophic current and rainfall and the Chl-a concentration during 2003–2020. The Chl-a concentration increased with increasing rainfall in August, i.e., the upwelling season. The rainfall was converted to runoff and flowed into the coastal waters. The Chl-a concentration in summer was mainly regulated by upwelling processes (Jing et al., 2011), with a negative correlation (Figures 4–5). Therefore, the increased precipitation and weaker upwelling processes could have induced the increased Chl-a concentration in the HEC

536   (upward arrow in Figure 13).

537

538
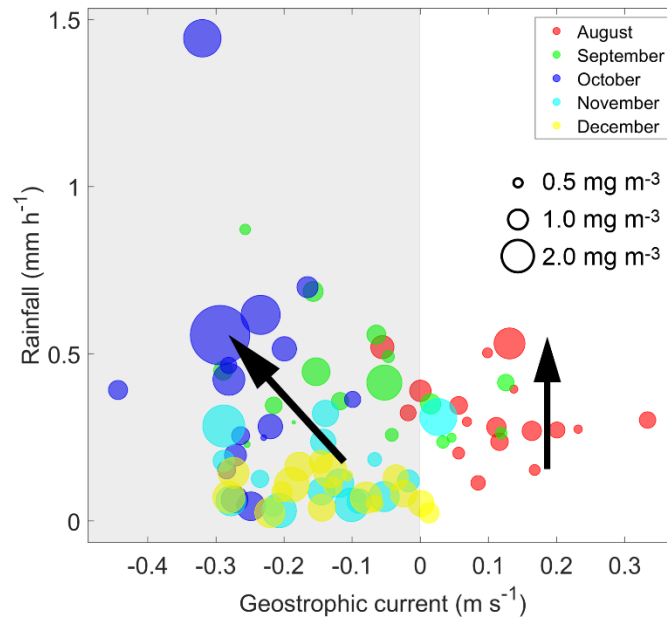
539   Figure 13. Bubble diagram showing the relationships between the geostrophic current and rainfall
540   and the Chl-a concentration. The size of the bubble represents the Chl-a concentration. The left
541   panel in grey represents the southwest along-shelf current in winter. The right panel represents the
542   northeast along-shelf current in summer. Black arrows represent the relationship between the
543   geostrophic current and rainfall and the Chl-a concentration.

544

545   In autumn and winter, the Chl-a concentration was increased by the increases in rainfall and
546   the northeastward coastal current (oblique upward arrow in Figure 13). In October, the heaviest
547   rainfall and the strongest current coincided with the highest Chl-a concentration. The coastward
548   wind component was strongest in October (Figure 2a), as was the northeast monsoon, which
549   induced coastward Ekman transport (Xuan et al., 2021). The downwelling movement transported
550   the nutrients from the rivers and the coastal current to the middle and under layers on the shelf,
551   which promoted an increase in silicate-favoring phytoplankton. The cruise data provide evidence
552   of the high Chl-a concentrations over the shelf (Figure 8h).

553

554   **5 Conclusions**
555   In this study, in situ observations and monthly satellite observations from 2003 to 2020 are
556   used to investigate the spatiotemporal variability in the Chl-a concentration in the HEC area.
557   Along-track satellite altimeter data for the continental shelf of the NWSCS were used to retrieve
558   the geostrophic current. In addition, cruise data obtained in October 2019 and July 2021 were used
559   to examine the vertical structure of the Chl-a concentration during the three observational seasons.
560   Driven by the prevailing monsoon, the SST of the core upwelling area (within a depth of 100
561   m) in summer increased, but its area decreased, which indicates that the UEH weakened during
562   the 18-year study period. The EOF analysis of the Chl-a concentration revealed that it exhibited
563   strong seasonal and interannual variability in the NWSCS. The climatological average Chl-a
564   concentration mostly peaked near the coast in autumn, 1.18 mg m^{-3}. However, the Chl-a

concentration in the core upwelling area was lowest during the upwelling season, approximately 0.74 mg m^{-3} in summer, which contradicts the previous conclusion of a high-productivity upwelling system.

ENSO events regulated the Chl-a concentration of the upwelling area through wind stress. The interannual variations in the spatial mean of the Chl-a concentration were consistent with the ENSO events. There was a positive correlation between the Chl-a anomalies and the La Niña events. In El Niño years, the Chl-a concentration decreased to a lower level in summer. However, the summer Chl-a concentration increases to as high as 1.0 mg m^{-3} with weak upwelling during El Niño years. In further research we will investigate the relationship between the Chl-a variability and ENSO in the HEC.

Both the along-shelf current from the north and precipitation were crucial factors controlling the Chl-a concentration in the UEH area. The downwelling movement transported nutrients from the rivers and the coastal current to the middle and lower layers on the shelf, which promoted an increase in silicate-favoring phytoplankton. These results provide scientific evidence for the development of the marine economy in the upwelling area.

Acknowledgments

The authors are grateful to the anonymous reviewers for their valuable suggestions and comments. This research was funded by the National Key Research and Development Program of China (2022YFC3104805); National Natural Science Foundation of China (42276019, 41476009, 41976200, 41506018, 41706025); Innovation Team Plan for Universities in Guangdong Province (2019KCXTF021); and First-class Discipline Plan of Guangdong Province (080503032101, 231420003).

Data Availability Statement

Kd490, Rrs645, Chl-a, SST, and PAR data were downloaded from Ocean Color Data Processing System (http://oceandata.sci.gsfc.nasa.gov/)

SSW, SSS, rainfall rate, and along-track SLA data were downloaded from CMEMS (https://marine.copernicus.eu/)

The shipboard sections data are archived at https://dx.doi.org/10.6084/m9.figshare.19679538.

The typhoon track was obtained from the Tropical Cyclone Data Center of the China Meteorological Administration (CMA) (http://tcdata.typhoon.org.cn).

Nino index was downloaded from Climate Prediction Center in National Weather Service. (https://origin.cpc.ncep.noaa.gov/products/analysis_monitoring/ensostuff/ONI_v5.php)

Author contributions

JYL, ML and LLX were responsible for writing the original draft. Review and editing were conducted by QAZ. Conceptualization was handled by JYL, QAZ and LLX. CW, YX and TYZ were responsible for data curation. LLX acquired funding.

Competing interests

The contact author has declared that none of the authors has any competing interests.

Disclaimer

611

612 **References**

613 Aoki, K., Kuroda, H., Setou, T., Okazaki, M., Yamatogi, T., Hirae, S., Ishida, N., Yoshida, K., Mitoya,
614 Y., 2019. Exceptional red-tide of fish-killing dinoflagellate Karenia mikimotoi promoted by typhoon-
615 induced upwelling. Estuarine Coastal and Shelf Science 219, 14-23.

616 Barua, D.K., 2005. Coastal Upwelling and Downwelling, in: Schwartz, M.L. (Ed.), Encyclopedia of
617 Coastal Science. Springer Netherlands, Dordrecht, pp. 306-308.

618 Cape, M.R., Straneo, F., Beaird, N., Bundy, R.M., Charette, M.A., 2019. Nutrient release to oceans
619 from buoyancy-driven upwelling at Greenland tidewater glaciers. Nature Geoence 12, 34-39.

620 Chen, F., Zhen, Z., Meng, Y., Zhu, Q., Xie, L., Zhang, S., Chen, Q., Chen, J., 2016. Diel variation of
621 nutrients and chlorophyll α concentration in the Qiongdong sea region during the summer of 2013.
622 Haiyang Xuebao 38, 76-83.

623 Deng, S., Zhong, H., Wang, M., Yun, F., 1995. On relation between upwelling off Qionghai and fishery.
624 Journal of Oceanography In Taiwan Strait 14, 51-56.

625 Ding, Y., Yao, Z., Zhou, L., Bao, M., Zang, Z., 2018. Numerical modeling of the seasonal circulation in
626 the coastal ocean of the Northern South China Sea. Frontiers of Earth Science 14, 90-109.

627 Gan, J., San Ho, H., Liang, L., 2013. Dynamics of Intensified Downwelling Circulation over a
628 Widened Shelf in the Northeastern South China Sea. Journal of Physical Oceanography 43, 80-94.

629 Garratt, J., 1977. Review of Drag Coefficients Over Oceans and Continents. Monthly Weather Review
630 105, 915-929.

631 Hersbach, H., Bell, B., Berrisford, P., Biavati, G., Horányi, A., Muñoz Sabater, J., Nicolas, J., Peubey,
632 C., Radu, R., Rozum, I., Schepers, D., Simmons, A., Soci, C., Dee, D., Thépaut, J.-N., 2018. ERA5
633 hourly data on single levels from 1959 to present. Copernicus Climate Change Service (C3S) Climate
634 Data Store (CDS) (Accessed on < 15-Dec-2022 >).

635 Hu, J., Wang, X.H., 2016. Progress on upwelling studies in the China seas. Reviews of Geophysics 54,
636 653– 673.

637 Hu, Q., Chen, X., Huang, W., Zhou, F., 2021. Phytoplankton bloom triggered by eddy-wind interaction
638 in the upwelling region east of Hainan Island. Journal of Marine Systems 214, 103470.

639 Huynh, H.-N.T., Alvera-Azcárate, A., Beckers, J.-M., 2020. Analysis of surface chlorophyll a
640 associated with sea surface temperature and surface wind in the South China Sea. Ocean Dynamics 70,
641 139-161.

642 Jing, Z., Qi, Y., Du, Y., 2011. Upwelling in the continental shelf of northern South China Sea associated
643 with 1997-1998 El Nino. Journal of Geophysical Research 116, C02033.

644 Jing, Z., Qi, Y., Du, Y., Zhang, S., Xie, L., 2015. Summer upwelling and thermal fronts in the
645 northwestern South China Sea: Observational analysis of two mesoscale mapping surveys. Journal of
646 Geophysical Research: Oceans 120, 1993-2006.

647 Jing, Z., Qi, Y., Fox-Kemper, B., Du, Y., Lian, S., 2016. Seasonal thermal fronts on the northern South
648 China Sea shelf: Satellite measurements and three repeated field surveys. Journal of Geophysical
649 Research: Oceans 121, 1914-1930.

650 Jing, Z., Qi, Y., Hua, Z.-l., Zhang, H., 2009. Numerical study on the summer upwelling system in the
651 northern continental shelf of the South China Sea. Continental Shelf Research 29, 467-478.

652 Kim, T.-W., Najjar, R.G., Lee, K., 2014. Influence of precipitation events on phytoplankton biomass in

coastal waters of the eastern United States. Global Biogeochemical Cycles 28, 1-13.

Kuo, N., Ho, C., Lo, Y., Huang, S., Tsao, C., 2008. Variability of chlorophyll-a concentration and sea surface wind in the South China Sea associated with the El Niño-Southern Oscillation, OCEANS 2008 - MTS/IEEE Kobe Techno-Ocean, pp. 1-5.

López Abbate, M.C., Molinero, J.C., Guinder, V.A., Perillo, G.M.E., Freije, R.H., Sommer, U., Spetter, C.V., Marcovecchio, J.E., 2017. Time-varying environmental control of phytoplankton in a changing estuarine system. Science of The Total Environment 609, 1390-1400.

Li, J., Zheng, H., Xie, L., Zheng, Q., Ling, Z., Li, M., 2021a. Response of Total Suspended Sediment and Chlorophyll-a Concentration to Late Autumn Typhoon Events in the Northwestern South China Sea. Remote Sensing 13, 2863.

Li, J., Zheng, Q., Hu, J., Xie, L., Zhu, J., Fan, Z., 2016. A case study of winter storm-induced continental shelf waves in the northern South China Sea in winter 2009. Continental Shelf Research 125, 127-135.

Li, J., Zheng, Q., Li, M., Li, Q., Xie, L., 2021b. Spatiotemporal Distributions of Ocean Color Elements in Response to Tropical Cyclone: A Case Study of Typhoon Mangkhut (2018) Past over the Northern South China Sea. Remote Sensing 13, 687.

Lin, P., Cheng, P., Gan, J., Hu, J., 2016. Dynamics of wind-driven upwelling off the northeastern coast of Hainan Island. Journal of Geophysical Research: Oceans 121, 1160-1173.

Liu, S.H., Li, J.G., Sun, L., Wang, G.H., Tang, D.L., Huang, P., Yan, H., Gao, S., Liu, C., Gao, Z.Q., Li, Y.B., Yang, Y.J., 2020. Basin-wide responses of the South China Sea environment to Super Ty-phoon Mangkhut (2018). Science of the Total Environment 731, 139093.

Liu, Y., Peng, Z., Shen, C.-C., Zhou, R., Song, S., Shi, Z., Chen, T., Wei, G., DeLong, K.L., 2013. Recent 121-year variability of western boundary upwelling in the northern South China Sea. Geophysical Research Letters 40, 3180-3183.

Ma, C., Zhao, J., Ai, B., Sun, S., 2021. Two-Decade Variability of Sea Surface Temperature and Chlorophyll-a in the Northern South China Sea as Revealed by Reconstructed Cloud-Free Satellite Data. IEEE Transactions on Geoscience and Remote Sensing 59, 9033-9046.

Mcgregor, H.V., Dima, M., Fischer, H.W., Mulitza, S., 2007. Rapid 20th-Century Increase in Coastal Upwelling off Northwest Africa. Science 315, 637-639.

Meng, F., Dai, M., Cao, Z., Wu, K., Zhao, X., Li, X., Chen, J., Gan, J., 2017. Seasonal Dynamics of Dissolved Organic Carbon Under Complex Circulation Schemes on a Large Continental Shelf: The Northern South China Sea. Journal of Geophysical Research: Oceans 122, 9415-9428.

Ning, X., Chai, F., Xue, H., Cai, Y., Liu, C., Shi, J., 2004. Physical-biological oceanographic coupling influencing phytoplankton and primary production in the South China Sea. Journal of Geophysical Research: Oceans 109.

North, G.R., Bell, T.L., Cahalan, R.F., Moeng, F.J., 1982. Sampling Errors in the Estimation of Empirical Orthogonal Functions. Monthly Weather Review 110, 699-706.

Qin, M., Li, D., Dai, A., Hua, W., Ma, H., 2018. The influence of the Pacific Decadal Oscillation on North Central China precipitation during boreal autumn. International Journal of Climatology 38, 821-831.

Shi, W., Huang, Z., Hu, J., 2021. Using TPI to Map Spatial and Temporal Variations of Significant Coastal Upwelling in the Northern South China Sea. Remote Sensing 13, 1065.

Song, X., Lai, Z., Ji, R., Chen, C., Zhang, J., Huang, L., Yin, J., Wang, Y., Lian, S., Zhu, X., 2012. Summertime primary production in northwest South China Sea: Interaction of coastal eddy, upwelling

697 and biological processes. Continental Shelf Research 48, 110-121.

698 Su, J., Xu, M.Q., Pohlmann, T., Xu, D.F., Wang, D.R., 2013. A western boundary upwelling system
699 response to recent climate variation (1960-2006). Continental Shelf Research 57, 3-9.

700 Thompson, P.A., O'Brien, T.D., Paerl, H.W., Peierls, B.L., Harrison, P.J., Robb, M., 2015. Precipitation
701 as a driver of phytoplankton ecology in coastal waters: A climatic perspective. Estuarine, Coastal and
702 Shelf Science 162, 119-129.

703 Wang, C., Wang, W., Wang, D., Wang, Q., 2006. Interannual variability of the South China Sea
704 associated with El Niño. Journal of Geophysical Research: Oceans 111.

705 Wang, L., Xie, L., Zheng, Q., Li, J., Li, M., Hou, Y., 2020. Tropical cyclone enhanced vertical transport
706 in the northwestern South China Sea I: Mooring observation analysis for Washi (2005). Estuarine,
707 Coastal and Shelf Science 235, 106599.

708 Wang, Y., Kang, J.-h., Liang, Q.-y., He, X.-b., Wang, J.-j., Lin, M., 2018. Characteristics of
709 phytoplankton communities and their biomass variation in a gas hydrate drilling area in the northern
710 South China Sea. Marine Pollution Bulletin 133, 606-615.

711 Xie, L., Zhang, S., Zhao, H., 2012. Overview of studies on Qiongdong upwelling. Journal of Tropical
712 Oceanography, 38-44.

713 Xu, D., Huang, H., Zheng, N., Zhang, J., Pan, A., 2020. Role of biological activity in mediating
714 acidification in a coastal upwelling zone at the east coast of Hainan Island. Estuarine Coastal and Shelf
715 Science 249.

716 Xuan, J., Ding, R., Ni, X., Huang, D., Chen, J., Zhou, F., 2021. Wintertime Submesoscale Offshore
717 Events Overcoming Wind-Driven Onshore Currents in the East China Sea. Geophysical Research
718 Letters 48, e2021GL095139.

719 Yang, C., Ye, H., 2022. Enhanced Chlorophyll-a in the Coastal Waters near the Eastern Guangdong
720 during the Downwelling Favorable Wind Period. Remote Sensing 14, 1138.

721 Yang, Y., Xie, S.-P., Du, Y., Tokinaga, H., 2015. Interdecadal Difference of Interannual Variability
722 Characteristics of South China Sea SSTs Associated with ENSO. Journal of Climate 28, 7145-7160.

723 Ye, H.J., Sui, Y., Tang, D.L., Afanasyev, Y.D., 2013. A subsurface chlorophyll a bloom induced by
724 typhoon in the South China Sea. Journal of Marine Systems 128, 138-145.

725 Yu, J.-Y., Zou, Y., Kim, S.T., Lee, T., 2012. The changing impact of El Niño on US winter
726 temperatures. Geophysical Research Letters 39.

727 Yu, Y., Wang, Y., Cao, L., Tang, R., Chai, F., 2020. The ocean-atmosphere interaction over a summer
728 upwelling system in the South China Sea. Journal of Marine Systems 208, 103360.

729 Zeng, D., Li, J., Xie, L., Ye, X., Zhou, D., 2022. Analysis of temporal characteristics of chlorophyll a in
730 Lingding Bay during summer. Journal of Tropical Oceanography 41, 16-25.

731 Zhang, J., Ren, J.L., Liu, S.M., Zhang, Z.F., Wu, Y., Xiong, H., Chen, H.T., 2003. Dissolved aluminum
732 and silica in the Changjiang (Yangtze River): Impact of weathering in subcontinental scale. Global
733 Biogeochemical Cycles 17, 1077.

734 Zhao, J., Barnes, B., Melo, N., English, D., Lapointe, B., Muller-Karger, F., Schaeffer, B., Hu, C.,
735 2013. Assessment of satellite-derived diffuse attenuation coefficients and euphotic depths in south
736 Florida coastal waters. Remote Sensing of Environment 131, 38-50.

737 Zheng, G.M., Tang, D.L., 2007. Offshore and nearshore chlorophyll increases induced by typhoon
738 winds and subsequent terrestrial rainwater runoff. Marine Ecology Progress Series 333, 61-74.

739 Zheng, M., Xie, L., Zheng, Q., Li, M., Chen, F., Li, J., 2021. Volume and Nutrient Transports Disturbed
740 by the Typhoon Chebi (2013) in the Upwelling Zone East of Hainan Island, China. Journal of Marine

741   Science and Engineering 9, 324.

742

743